Dalton Transactions

Accepted Manuscript

ROYAL SOCIETY OF CHEMISTRY

www.rsc.org/dalton

Phase control of a perovskite transition-metal oxide through oxygen displacement at heterointerface

Daisuke Kan[1*], Ryotaro Aso[1], Hiroki Kurata[1] and Yuichi Shimakawa[1,2]

[1]Institute for Chemical Research, Kyoto University, Uji, Kyoto 611-0011 Japan

[2]Japan Science and Technology Agency, CREST, Uji, Kyoto 611-0011, Japan

*dkan@scl.kyoto-u.ac.jp

Abstract

Controlling structural distortions that are closely related to functional properties in transition-metal oxides is a key not only to exploring novel phenomena but also to developing novel oxide-based electronic devices. In this review article, we overview investigations revealing that oxygen displacement at the heterointerface is a key parameter characterizing structure-property relationships of heterostructures. We further demonstrate the interface engineering of the oxygen displacement is useful to control structural and electronic properties of strained oxides.

1. Introduction

Complex electronic structures responsible for a wide variety of functional properties seen in transition-metal oxides often emerge when slight structural distortions are introduced in the basic crystal structures. Exploring the possibility to manipulate structural distortions that underpin functional properties has therefore been a central research topic in fundamental materials science and in applications of oxides in electronic devices[1,2,3,4,5,6,7,8,9,10,11,12,13,14,15,16,17,18,19]. For perovskite oxides ABO_3, the lattice of which consists of a three dimensional network of corner-sharing oxygen octahedra that each has a transition metal atom at its center, distortions in the octahedral network result in changes in the metal-oxygen bonding environment that are associated with extra displacements of the oxygen atoms and consequently have an impact on functional properties through the metal-oxygen orbital hybridizations.

Heterostructures and superlattices consisting of different ABO_3 oxides provide an exciting platform for not only exploring but also controlling the functional properties[20,21,22,23,24,25,26,27]. Such artificial structures are fabricated by coherently growing dissimilar oxides in such a way that the in-plane lattice parameters of the film layers are identical to those of the substrate. This introduces additional structural distortions as a result of accommodation of elastic strain energy due to structural mismatch at the heterointerface. An atomic-scale understanding of how structural distortions are introduced to accommodate the structural mismatch at the heterointerface, however, is missing because precise measurements of positions of the oxygen atoms are experimentally difficult and challenging.

Recent theoretical works[27,28,29] have showed that even in coherently-grown films of which in-plane lattice parameters are fixed by substrate lattices, there are still degrees of freedom in the oxygen atomic positions, namely octahedral distortions including deformation and tilts (or rotations) in the perovskite lattice framework. In fact, there have been reports[16,30,31,32,33,34,35,36] that

iso-compositional oxide films coherently grown on a substrate can have various structures with different octahedral tilt patterns. This raises a possibility that different types of structural phase can be stabilized by adjusting the oxygen atomic positions. These highlight an importance to visualize oxygen coordination environments that characterize oxygen octahedral distortions accommodated in coherently-grown heterostructures. It is also crucial to develop a way to engineer oxygen environments in the heterostructures.

In this review article, we overview recent theoretical and experimental investigations that provide atomic-level insights on octahedral distortions in oxide heterostructures. We begin with a brief summary of theoretical investigations on oxygen octahedral distortions in oxide heterostructures, emphasizing an importance of direct observations of oxygen coordination environments. We then overview several experimental techniques that provide information on the oxygen octahedral distortions, including high-resolution annular bright-field (ABF) imaging in scanning transmission electron microscopy (STEM). This is followed by the discovery that a $SrRuO_3$ (SRO) layer in the heterostructure has structure-property relationships characterized by the oxygen displacement at the heterointerface[37,38,39,40,41,42]. We also show that the interfacial oxygen displacement can be engineered, and thus the SRO phase can be controlled, by inserting a one-unit-cell-thick $BaTiO_3$ (BTO) layer into the heterointerface. Based on these experimental results and recent investigations regarding octahedral distortions in oxide heterostructures, we discuss the importance of the interfacial oxygen displacement, which characterizes octahedral connection at the interface, in controlling structural and physical properties of heterostructures.

2. Theoretical insights on oxygen octahedral distortions in oxide heterostructures

Theoretical approach based on first-principles density-functional calculations has been recognized as a powerful tool for investigating and understanding structure-property relationships of

complex transition metal oxides[1,43,44,45,46,47,48,49]. It has been revealed that distortions of oxygen octahedra including deformations and tilts (or rotations) are closely tied with physical properties, underscoring an importance of engineering such octahedral distortions. Substrate-induced strain, which imposes an in-plane new lattice parameter on a film, is often used to modify octahedral distortions and consequently physical properties. Recent theoretical works[27,28,29] implied that the corner-sharing networks of oxygen octahedra in oxides display flexible responses to the strain. The substrate-induced change in in-plane lattice parameter could be accommodated by a change in in-plane metal-oxygen bond lengths and/or magnitudes and types of octahedral tilt (or metal-oxygen bond angle), which are associated with displacements of the oxygen atoms from the original positions. An important consequence of the substrate-induced modifications of octahedral distortions is that various structural phases with different oxygen coordination environments are stabilized.

It was also theoretically proposed[29] that octahedral distortions, especially octahedral tilts in the substrate, can be propagated into a film across the heterointerface and that this is a promising way to stabilize a structural phase with novel oxygen coordinations not seen in bulk. A theoretical calculation[29] showed that while bulk $SrFeO_3$ has an ideal cubic perovskite structure with no octahedral tilt ($a^0a^0a^0$), the $a^0a^0c^-$ octahedral tilt can be introduced into $SrFeO_3$ by heterostructuring it with $SrTiO_3$ that has the ground state of a tetragonal structure with the $a^0a^0c^-$ TiO_6 octahedral tilt. An implication of these calculation results is that the oxygen displacement at the interface, which characterizes octahedral connections between two oxides with different distortions, is a key in controlling and further exploring structural and electronic properties of strained films, underscoring the significance of direct observations of oxygen octahedral distortions, namely oxygen coordination environments in oxide heterostructures. This also highlights the importance for delineating how interface structures including oxygen displacements underpin structure-property relationships of strained oxide films.

3. Direct observations of oxygen octahedral distortions in oxide heterostructures by ABF-STEM

To evaluate oxygen octahedral distortions in oxide heterostructures, positions of both cations and oxygen have to be precisely determined. Such atomic-level information is in principle obtained by structural analysis based on either synchrotron x-ray diffractions or (S)TEM observations.

Synchrotron x-ray measurements of multiple crystal truncation rods (CTRs) and their analysis[50,51,52,53,54,55] allow for constructions of three-dimensional and sub-Ångström-resolution maps of the electron density (or the atomic position) in oxide heterostructures, providing insights on oxygen octahedral distortions. However, the data analysis is rather complex, which have limited wide-spread use of the CTR-based approach. Recently it was proposed[56,57] that oxygen octahedral tilts in heterostructures can be quantified by reproducing a set of half-order Bragg reflection intensities arising from oxygen displacements from the original positions in the ideal cubic lattice. This technique was applied to various coherently-grown heterostructures and superlattices[56,58,59,60] consisting of perovskite oxides such as $LaNiO_3$ and $SrMnO_3$. For $LaNiO_3$[56] which has a rhombohedral structure with an $a^-a^-a^-$ octahedral rotation pattern ($\alpha = \beta = \gamma = 5.2^o$) in bulk, the tensile strain (grown on an $SrTiO_3$ substrates) decreases γ while increasing α and β ($\alpha = \beta = 7.1^o$ and $\gamma = 0.3^o$). The compressive strain (grown on an $LaAlO_3$ substrate), on the other hand, increases γ while decreases α and β ($\alpha = \beta = 1.7^o$ and $\gamma = 7.9^o$). These observations show that octahedral tilt in the heterostructure is distinct from the bulk counterpart, highlighting the important role of the substrate-induced strain on octahedral tilts[56,61,62].

While the x-ray-diffraction-based approaches reveal important aspects of octahedral distortions and atomic structures in heterostructures, precise determination of the octahedral

distortions, in particular across heterointerface where influences of the structural mismatch are dominant, remains challenging. Each constituent layer in heterostructures is not necessarily *uniform* in the octahedral distortions and local structure analysis like identifications of gradual changes in tilt angles across the interface is important. Aberration-corrected (S)TEM based approaches[16,19,63,64,65,66,67,68,69,70,71] allow for not only qualitative but also quantitative determinations of the atomic positions and provide atomic-level views on octahedral distortions in heterostructures. Atomic-resolution observations of all constituent atoms including oxygen in heterostructure was successfully demonstrated by using negative spherical-aberration (Cs)-corrected TEM[65,66,67]. For the TEM observations, however, the image contrast is very sensitive to defocus value and sample thickness. The proper interpretations of the obtained images therefore require intricate image simulations.

Recent development of ABF imaging in Cs-corrected STEM enables simultaneous imaging of both light and heavy elements[72,73,74]. In contrast to the conventional TEM technique, the ABF image contrast in STEM is relatively insensitive to the sample thickness[72,73], allowing for intuitive interpretation of obtained images. ABF imaging combined with high-angle annular dark-field (HAADF) imaging in which the contrast strongly depends on atomic number (Z)[75,76] would be therefore appropriate to visualize both cation and oxygen atoms in oxide heterostructures. However one drawback with the STEM-based approach is that the image is often distorted due to drifts of both a specimen and an incident probe, which makes it difficult to extract atomic positons. In order to overcome this problem and obtain high-resolution STEM images with minimized image distortion, we employed fast multiple-image acquisition and drift correction techniques using cross correlation of the images[77]. Atomic positions were then determined with sub-Ångström precision from the obtained image by using Bragg filtering and cubic interpolation techniques[78,79].

To obtain atomic-level insight on oxygen octahedral distortions in the heterostructure, we

here focus on a heterostructure consisting of SRO[80] and $GdScO_3$ (GSO). Both SRO and GSO have *Pbmn* orthorhombic perovskite structures ($\sqrt{2}a_{pc} \times \sqrt{2}a_{pc} \times 2a_{pc}$) with in-phase octahedral rotations around the $[001]_{ortho}$ axis and out-of-phase rotations around the $[110]_{ortho}$ and $[1\text{–}10]_{ortho}$ axis. (The subscripts *pc* and *ortho* denote for the pseudocubic and orthorhombic perovskite notations, respectively). The rotation pattern is described as $a^-a^-c^+$ in the Glazer notation[81]. Given the large difference in the oxygen octahedral tilt angle θ_{tilt} (θ_{tilt_SRO} = 168°, θ_{tilt_GSO} = 156°) as well as the lattice parameters (SRO; a_{pc_SRO} = 3.92 Å, GSO; a_{pc_GSO} = 3.96 Å)[82,83], the additional displacements of the oxygen atoms would be induced at the SRO/GSO heterointerface to maintain the corner connection between the RuO_6 and ScO_6 octahedra by sharing the oxygen atoms (Fig. 1). Thus, the SRO/GSO heterostructure can be considered as a representative model heterostructure to investigate how structural distortions are introduced as a result of structural mismatches in the lattice parameter and the octahedral tilt angle.

Shown in Figure 2 are typical high-resolution HAADF- and ABF-STEM images of the SRO/GSO heterostructure[40]. Both images were taken along the $[001]_{ortho}$ direction because the oxygen octahedra have in-phase rotations around this direction. The HAADF image (Fig. 2a) of which *Z*-contrasts are in good agreement with the simulated contrasts in the inset, shows that the SRO layer is coherently grown on GSO and that there are no misfit dislocations in the heterostructure. This is consistent with our previous x-ray structural characterizations[40]. Based on HAADF-intensity profile analysis (Fig. 2b), the termination layer of GSO at the heterointerface is identified to be a ScO_2 layer[84] and the SRO layer begins from the SrO layer. Fig. 2c shows the ABF image taken from the same region as the HAADF image (Fig. 2a), where the atomic positions are visualized as dark contrast. In the image we can clearly see not only the cation but also oxygen atomic columns, providing projected shapes of the octahedra as denoted by the red open squares. This is also verified from the simulated images in the inset of Fig. 2c.

4. Structure-property relationships of $SrRuO_3$ dictated by oxygen displacements at heterointerface

Having established the technique of obtaining STEM images with minimized image distortions, which is suitable for precise determinations of both cation and oxygen atomic positions in heterostructures, we investigated the origin of the thickness-dependent monoclinic-tetragonal structural transition observed for the SRO layer in the SRO/GSO heterostructure by tracking changes in oxygen atomic positions upon the transition. Previous x-ray structural characterizations[40] showed that upon the structural phase transition taking place at 16 nm in the SRO layer thickness, there was no difference in the in-plane lattice spacing, suggesting that the transition is driven by changes in the oxygen octahedral tilt in the strained SRO layers.

Fig. 3 shows variations of the out-of-plane lattice spacing (d_{out}) and oxygen octahedral tilt angle (θ_{tilt}) in the monoclinic SRO/GSO (m-SRO/GSO) and tetragonal SRO/SGO (t-SRO/GSO) heterostructures. The lattice spacing and tilt angle were extracted from the A-site cation positions in the HAADF images and the oxygen atomic positions in the ABF images, respectively. The d_{out} of the m-SRO layer is slightly larger than that of the t-SRO layer and the out-of-plane and in-plane θ_{tilt} of the t-SRO layer are smaller than those for the m-SRO layer. This is consistent with the thickness-dependent change in d_{out} of the films determined from the x-ray diffraction analysis[40]. We note that the variation of the out-of-plane θ_{tilt} exhibits essentially the same trend as that of the in-plane θ_{tilt}, regardless of the structural phase of the SRO layers (Fig. 3).

We also found that the observed difference in the octahedral tilt in the SRO layer originates from the changes in octahedral connections across the heterointerface between SRO and GSO. Fig. 4 plots the in-plane displacement Δx of the apical oxygen atom, which is directly related to the octahedral tilt. The definition of Δx is shown in the figure. For the m-SRO/GSO

heterostructure, the oxygen shared by the RuO_6 and ScO_6 octahedra at the interface has Δx of 26 pm, which is larger than that for the m-SRO layer region away from the interface, and as a consequence, Δx of the m-SRO layer remains almost comparable to the bulk SRO value (21 pm). In contrast, for the t-SRO/GSO heterostructure, Δx at the interface is reduced to 19 pm and Δx of the t-SRO layer is about 9 pm smaller than that of m-SRO. The reduction in Δx is consistent with the observation of the suppression of the octahedral tilt of the t-SRO layer (Fig. 3).

These observations point to a conclusion that the relaxation of the octahedral tilts induced by the substrate is the origin for the (thickness-dependent) monoclinic-tetragonal structural transition for the SRO/GSO heterostructure. This is schematically shown in Fig. 4b. When the SRO layer thickness is below 16 nm, the oxygen displacement larger than the bulk SRO is maintained at the interface, which facilitates the propagation of the octahedral tilt from the substrate and as a result the m-SRO layer with the tilted RuO_6 octahedra is stabilized, although the monoclinic structure is energetically unfavorable. With further increasing the SRO layer thickness, the SRO lattice is no longer tolerant for the accumulation of the energy increased by the monoclinic octahedral distortions and, consequently the lattice releases the additional energy by relaxing the substrate-induced octahedral tilt, leading to the appearance of the t-SRO structure. This is associated with the reduction in the in-plane displacement of the oxygen shared between the RuO_6 and ScO_6 octahedra in such a way that the octahedral tilt propagation from the substrate is blocked at the interface. This indicates that the oxygen displacement at the interface (highlighted with yellow boxes in Fig. 4b), which characterizes the interfacial octahedral connection, is closely related to the structural phase of the strained SRO layer.

Strong influence of the interfacial octahedral connection on film's structural phase is also recently reported[85,86,87] for oxide films grown on cubic $(LaAlO_3)_{0.3}(Sr_2AlTaO_6)_{0.7}$ (LSAT) and orthorhombic $NdGaO_3$ (NGO) substrates. For $La_{0.5}Sr_{0.5}CoO_3$[87], a structural phase with CoO_6

octahedral tilts is favorably stabilized when the films were grown on the NGO substrate. On the other hand, a structural phase with suppressed tilts is seen when grown on the LSAT substrate. Given that LSAT and NGO have almost the same lattice parameter and differ in the octahedral tilt pattern ($a^0a^0a^0$ for LSAT and $a^-a^-c^+$ for NGO), the observed difference in the film's structure can be attributed to the difference in the interfacial octahedral connections. As discussed below, interfacial octahedral connection has also strong influence on physical properties of films. Detailed analysis on octahedral connections at $La_{0.7}Sr_{0.3}MnO_3/SrTiO_3$ heterointerface[88] have shown that the MnO_6 octahedral tilt is largely suppressed at the interface. Considering that $SrTiO_3$ has non-tilted TiO_6 octahedra, this result is possibly another implication that the oxygen displacement plays the important role in determining interfacial octahedral connections.

Magneto-transport properties of the SRO/GSO heterostructure were further characterized to see how the structural change of the SRO layer influences functional properties. Results are summarized in Fig. 5 revealing a concomitant change in magnetic anisotropy with the SRO layer structure. While both m- and t-SRO layers exhibit metallic conductions down to 10 K with a kink in the electrical resistivity vs. temperature (ρ_{xx}-T) curve due to the ferromagnetic transition around 100-130 K[40], the anomalous part (ρ_{AHE}) of the Hall resistivity (ρ_{xy}) is strongly dependent on the SRO layer structure as shown in Fig. 5a. For the m-SRO/GSO heterostructure, the square-shaped hysteresis due to the field-induced magnetization reversal is seen, confirming the ferromagnetic ordering in the m-SRO layer and its magnetic moment having a component along the $[110]_{GSO}$ (out-of-plane) direction. On the other hand, ρ_{AHE} for the t-SRO/GSO heterostructure exhibits no hysteresis, indicating that the magnetic moment in the t-SRO layer aligns along the in-plane direction. To determine the direction of the magnetic easy axis (E_a) in the SRO layer, we also measured the field angle (θ_H) dependence of ρ_{xx} and ρ_{xy}[40,42]. For materials with the strong magnetic anisotropy, such as SRO[89,90,91,92,80], the field-induced reversal of the magnetic moment takes place

only when the angle between E_a and the magnetic field exceeds 90°. The occurrence of the magnetic moment reversal can be observed as peaks in ρ_{xx} and jumps in ρ_{xy}. The typical results for the m-SRO/GSO and t-SRO/GSO heterostructures are shown in Fig. 5b and c respectively. Both m- and t-SRO layers exhibit the clear jumps in ρ_{xy} with the hysteresis in the clockwise and counter-clockwise field rotations due to the field-induced magnetization reversal. The jump in ρ_{xy} is observed at every 180° in θ_H, revealing the uniaxial magnetic anisotropy of the SRO layer. From the center position of the hysteresis, the E_a angles α for the m-SRO and t-SRO layers are determined to be ~45° and 90° tilted from the $[110]_{ortho}$ direction, respectively. Fig. 5d shows the thickness dependence of α of the SRO layer. There is no obvious thickness dependence in α for both m- and t-SRO layer. Instead, the E_a direction changes in response to the structural change of the SRO layer. The E_a of the m-SRO layer is tilted by ~45° from the $[110]_{ortho}$ direction while for the t-SRO layer the E_a is along the $[1\text{–}10]_{GSO}$ direction (the in-plane direction). This indicates that the E_a direction of SRO is primarily determined by the magnetocrystalline effect. The results indicate the impact of the octahedral tilts, namely the oxygen coordination environments on the magneto-transport properties of SRO, highlighting the significance of the interfacial oxygen displacement as a determining factor for the structure-property relationships. We note that strong influence of the octahedral tilts on functional properties including ferroelectric and magnetic properties has been revealed for various oxide films[16,86,87]. These implies that the structure-property relationship can be controlled through oxygen coordination environments in oxide heterostructures.

5. Phase control of $SrRuO_3$ through octahedral tilt propagation controlled by the interface engineering of the oxygen displacement

Having understood that the interfacial oxygen displacement in the SRO/GSO heterostructure, which characterizes the propagation of the octahedral tilts and consequently the

RuO_6 octahedral distortions, is a key for the structure-property relationships of the SRO layer, we next think about manipulating the oxygen displacement by engineering the interface structure, not by changing the thickness of the SRO layer. For perovskite oxides ABO_3, the in-plane displacement of the apical oxygen atom can be controlled by adjusting the octahedral tilt angle through the relative size mismatch between the A-site and B-site cations[93,94]. In fact, our high-resolution ABF-STEM observations of $ATiO_3$/GSO (A = Ba, Sr, $Sr_{0.7}Ca_{0.3}$ and $Sr_{0.5}Ca_{0.5}$) heterostructures[39] have revealed that the A-site cation size is a controlling parameter for the displacement of the oxygen atom shared by the TiO_6 and ScO_6 octahedra at the heterointerface. When the A-site cation size is relatively large, for example A = Ba, the interfacial oxygen displacement is negligibly small, blocking the octahedral tilt propagation at the heterointerface. This stabilizes the connections between the TiO_6 and ScO_6 octahedra with negligibly small tilts and as a result no octahedral tilts are seen in the $ATiO_3$ (A = Ba) layer.

Based on this, we propose an idea of the phase control of the SRO layer through the interface engineering of the oxygen displacement as schematically shown in Fig. 6. The insertion of a one-unit-cell-thick BTO layer between the SRO layer and GSO substrate would result in the formation of non-tilted RuO_6-TiO_6 octahedral connections with negligibly small oxygen displacement at the interface. This consequently stops the octahedral tilt propagation from the GSO substrate to the SRO layer and stabilizes the tetragonal SRO layer, unlike the monoclinic one that is seen when the SRO layer (below 16 nm) is directly grown on the GSO substrate.

To demonstrate the idea, we fabricated the SRO/BTO/GSO heterostructure whose thicknesses of the BTO layer and the SRO layer are 0.4 (corresponding to the thickness of the single unit cell) and 10-12 nm (referred to hereafter as SRO/1u.c.BTO/GSO), respectively. During the deposition, the thickness of the BTO layer was controlled by monitoring the oscillation of reflection high energy electron diffraction (RHEED) spot intensity as shown in Fig. 7a. The recovery of the

intensity confirms the two-dimensional growth of the BTO layer. In the bottom of the figure the RHEED patterns taken at the deposition temperature (700 ºC) for the GSO substrate and for the one-unit-cell-thick BTO layer deposited on the substrate are presented. The $(0\ 1/2)_{pc}$ spot resulting from the ScO_6 octahedral tilts in the substrate disappears after the deposition of the one-unit-cell-thick BTO layer, implying strong suppression of the octahedral tilts in the BTO layer.

Figs. 7b and 7c represent x-ray reciprocal space mappings taken from the m-SRO/GSO and SRO/1u.c.BTO/GSO heterostructures, revealing that the inserted BTO layer has the strong impact on the SRO layer structure. An important observation is that the SRO $(620)_{ortho}$ and $(260)_{ortho}$ reflections for the m-SRO/GSO heterostructure (Fig. 7b), appear at different positions along the out-of-plane direction (the vertical axis) while all SRO reflections for the SRO/1u.c.BTO/GSO heterostructure are also seen at the same position. This indicates that the insertion of the one-unit-cell-thick BTO layer stabilizes the tetragonal SRO layer. We note that the stabilization of the tetragonal SRO in the SRO/BTO/GSO heterostructure is independent of the BTO layer thickness[38] implying the significant roles of the SRO/BTO interface on the stabilization of the SRO tetragonal structure.

To obtain an atomic-level view how the one-unit-cell-thick BTO layer stabilizes the tetragonal SRO layer, we carried out cross-sectional HAADF- and ABF-STEM observations of the SRO/1u.c.BTO/GSO heterostructure. Figs. 8a and 8b show the HAADF-STEM image and the corresponding HAADF intensity (*Z*-contrast) profiles, respectively. While the *Z*-contrasts of BTO and GSO are similar with each other, the profiles in Fig. 8b show that the SRO/BTO interface is chemically sharp and that the termination layer of the BTO layer is a TiO_2 layer, indicating that the B-site termination is preserved in the entire heterostructure.

The ABF-STEM image of the SRO/1u.c.BTO/GSO heterostructure is presented in Fig. 9a. While the image contrast corresponding to the Gd atomic column right below the topmost ScO_2

layer is slightly distorted due to the ScO_6 octahedral tilts, no such distortion is seen in the contrast corresponding to the Ba atomic column in the one-unit-cell-thick BTO layer. This implies the formation of the octahedral connection between the non-tilted TiO_6 octahedra and the ScO_6 one at the interface. To qualitatively understand the octahedral connection across the interface, we plot the octahedral tilt angle θ_{tilt} and the in-plane oxygen displacement Δx against the atomic rows in the heterostructure in Figs. 9b and 9c respectively. We see the sudden decrease in the octahedral tilts in the BTO layer and the negligibly small RuO_6 octahedral tilts in the SRO layer. This is consistent with the fact that the SRO layer has the tetragonal structure. The reduced RuO_6 octahedral tilts in the SRO layer are attributed to the decrease in the in-plane oxygen displacement at the SRO/BTO interface as shown in Fig. 9c. The results indicate that the RuO_6-TiO_6 octahedral connection with negligibly small oxygen displacement at the interface blocks the propagation of the octahedral tilt from the GSO substrate, stabilizing the tetragonal SRO layer. It is also interesting to note that the only one-unit-cell-thick BTO layer is thick enough to completely block the tilt propagation.

The magneto-transport properties of the SRO/1u.c.BTO/GSO heterostructure is summarized in Fig. 10, revealing that the interface engineering of the oxygen displacement has the strong influence on the magnetic anisotropy in the SRO layer. Fig. 10a shows the field-dependence of ρ_{xy}. The anomalous Hall effect for the SRO/1u.c.BTO/GSO heterostructure is characteristic with in-plane magnetic anisotropy in contrast to that observed for the m-SRO/GSO heterostructure. To further determine the magnetic E_a direction α in the SRO/1u.c.BTO/GSO, we measured the in-plane magnetic field angle θ_H dependence of ρ_{xx}. The result in Fig. 10b shows that ρ_{xx} displays the peaks resulting from the field-induced magnetization reversal and that the center between the peaks in the clockwise and counter-clockwise field rotation is located at $\theta_H = \pm 90^o$. This indicates that the magnetic E_a of the SRO layer in the SRO/1u.c.BTO/GSO heterostructure is parallel to the $[1\text{–}10]_{ortho}$ direction (the in-plane direction) of the substrate. This is in contrast to the fact that the E_a direction

of the m-SRO layer grown directly on the GSO substrate is tilted by ~45º from the $[110]_{ortho}$ direction (the out-of-plane direction). The observed magneto-transport properties of the SRO/1u.c.BTO/GSO heterostructure are essentially the same as those of the tetragonal SRO layer (thicker than 16 nm) grown directly on the GSO substrate (see Fig. 5). The results indicate that the one-unit-cell-thick BTO layer between SRO and GSO results in the formation of the interfacial octahedral connection with the suppressed in-plane oxygen displacement stabilizing the tetragonal SRO. We also note that, as shown in Fig. 10c, the E_a direction in both the m-SRO/GSO and SRO/1u.c.BTO/GSO heterostructures is temperature independent. We further show in Fig. 10d that, regardless of the BTO layer thickness, the BTO layer insertion stabilizes the in-plane magnetic anisotropy in the SRO layer. All the results presented here demonstrate that the interface engineering of the oxygen displacement has the strong impact on the structural and magneto-transport properties of the SRO layer.

The importance of the interface structure on the octahedral tilts was also demonstrated for $BiFeO_3/La_{0.7}Sr_{0.3}MnO_3$ heterostructures[16]. The FeO_6 octahedral tilts in $BiFeO_3$ were found to strongly depend on a terminating layer (MnO_2 or (La,Sr)O) of $La_{0.7}Sr_{0.3}MnO_3$. While the bulk-equivalent octahedral tilt is maintained in the $BiFeO_3$ films on the MnO_2-terminated $La_{0.7}Sr_{0.3}MnO_3$, strongly suppressed tilts are stabilized in the film on the (La,Sr)O-terminated $La_{0.7}Sr_{0.3}MnO_3$. These termination-controlled octahedral tilts consequently allow for stabilizing distinct polar order from that seen in $BiFeO_3$ with the bulk-equivalent tilt. The $BiFeO_3$ film on the (La,Sr)O-terminated $La_{0.7}Sr_{0.3}MnO_3$ has suppressed polarizations and properties characteristics of anti-ferroelectric, unlike ferroelectric for bulk $BiFeO_3$.

Influence of interfacial modulations of octahedral tilt on magnetic phase transition behavior has also recently investigated for isovalent manganite superlattices $[(La_{0.7}Sr_{0.3}MnO_3)_n/(Eu_{0.7}Sr_{0.3}MnO_3)_n]\times m$[95]. It has shown that the superlattice period is a key

parameter for controlling magnetic behaviors. The superlattices whose period is larger than the length scale for the octahedral tilt modulations at the interface have a spatially-modulated magnetization. The short-period superlattices, on the other hand, exhibit a more uniform magnetization. These magnetic behaviors can be attributed to a systematic change in the Curie temperature underpinned by the modulated octahedral tilts in the superlattices. These results indicate that interfacially-engineered spatial modulations of octahedral distortions are a promising way to tailoring physical properties of oxides.

The interface engineering of the octahedral tilts can also be used to change the structural symmetry of the surface, allowing for controlling domain structures in oxide thin films under a given fixed strain. For a rhombohedrally-distorted ferroic $BiFeO_3$[34] that has a total of four energetically degenerate structural variants, two-variant domain structures are selectively formed when the film is directly grown on (110)-oriented orthorhombic perovskite substrates with octahedral tilts, such as $DyScO_3$. Four-variant domain structures are, on the other hand, recovered when the $SrTiO_3$ buffer layer with non-tilted TiO_6 octahedra, which would block the tilt propagation from the substrate, is inserted between the film and the substrate. These results demonstrate the usefulness of the interface engineering of octahedral tilts (or oxygen displacement) as a promising route for controlling structural and physical properties of oxide thin films.

5. Concluding remarks and future perspectives

We overview the significance, with regard to structural and functional properties of oxide heterostructures, of the oxygen displacement at the interface. For the SRO/GSO heterostructure, the interfacial oxygen displacement, which characterizes connection angle between the RuO_6 and ScO_6 octahedra at the interface, is closely correlated with the structural and magneto-transport properties of the SRO layer. This finding led us to the idea of controlling the phase of the SRO layer by

engineering the interfacial oxygen displacement. By inserting the one-unit-cell-thick BTO layer between the SRO layer and the GSO substrate, the oxygen displacement is largely suppressed at the interface and as a result even an SRO layer with a thickness such that the monoclinic phase is seen without the BTO layer is in the tetragonal phase. The observations show that manipulating the oxygen displacement at the heterointerface is a good way to control structural and electronic properties of strained oxides.

The results highlighted in this review demonstrate that a variety of oxygen coordination environments can be accommodated in heterostructures and that the oxygen environments in entire constituent layers can be controlled by adjusting only the interface structure. The idea of the interface engineering of the oxygen displacement could be feasibly applied to any other oxide materials as well as oxide-based devices such as transistors[96] and memory cells[97,98,99]. While visualizing and understanding oxygen coordination environments in heterostructures require cutting-edge experimental characterizations based on (S)TEM and synchrotron x-ray diffraction, designing and fabricating oxide heterostructures with novel oxygen coordination environments not seen in bulk materials are good ways to exploit the full potentials of oxides and further explore functionalities useful for electronic devices.

Acknowledgements

This work was partially supported by a Grant-in-Aid for Scientific Research (Grant No. 24760009), and a grant for the Joint Project of Chemical Synthesis Core Research Institutions from the Ministry of Education, Culture, Sports, Science and Technology of Japan. The work was also supported by the Japan Science and Technology Agency, CREST.

References

1. K. J. Choi, M. Biegalski, Y. L. Li, A. Sharan, J. Schubert, R. Uecker, P. Reiche, Y. B. Chen, X. Q. Pan, V. Gopalan, L. Q. Chen, D. G. Schlom and C. B. Eom, *Science*, 2004, **306**, 1005-1009.
2. J. H. Haeni, P. Irvin, W. Chang, R. Uecker, P. Reiche, Y. L. Li, S. Choudhury, W. Tian, M. E. Hawley, B. Craigo, A. K. Tagantsev, X. Q. Pan, S. K. Streiffer, L. Q. Chen, S. W. Kirchoefer, J. Levy and D. G. Schlom, *Nature*, 2004, **430**, 758-761.
3. J. H. Lee, L. Fang, E. Vlahos, X. Ke, Y. W. Jung, L. F. Kourkoutis, J.-W. Kim, P. J. Ryan, T. Heeg, M. Roeckerath, V. Goian, M. Bernhagen, R. Uecker, P. C. Hammel, K. M. Rabe, S. Kamba, J. Schubert, J. W. Freeland, D. A. Muller, C. J. Fennie, P. Schiffer, V. Gopalan, E. Johnston-Halperin and D. G. Schlom, *Nature*, 2010, **466**, 954-958.
4. R. J. Zeches, M. D. Rossell, J. X. Zhang, A. J. Hatt, Q. He, C. H. Yang, A. Kumar, C. H. Wang, A. Melville, C. Adamo, G. Sheng, Y. H. Chu, J. F. Ihlefeld, R. Erni, C. Ederer, V. Gopalan, L. Q. Chen, D. G. Schlom, N. A. Spaldin, L. W. Martin and R. Ramesh, *Science*, 2009, **326**, 977-980.
5. S. J. May, P. J. Ryan, J. L. Robertson, J. W. Kim, T. S. Santos, E. Karapetrova, J. L. Zarestky, X. Zhai, S. G. E. te Velthuis, J. N. Eckstein, S. D. Bader and A. Bhattacharya, *Nat. Mater.*, 2009, **8**, 892-897.
6. A. HarringtonSophie, J. Zhai, S. Denev, V. Gopalan, H. Wang, Z. Bi, A. T. RedfernSimon, S.-H. Baek, C. W. Bark, C.-B. Eom, Q. Jia, M. E. Vickers and J. L. MacManus-Driscoll, *Nat. Nano.*, 2011, **6**, 491-495.
7. S. Farokhipoor, C. Magen, S. Venkatesan, J. Iniguez, C. J. M. Daumont, D. Rubi, E. Snoeck, M. Mostovoy, C. de Graaf, A. Muller, M. Doblinger, C. Scheu and B. Noheda, *Nature*, 2014, **515**, 379-383.
8. A. Ohtomo and H. Y. Hwang, *Nature*, 2004, **427**, 423-426.
9. D. A. Muller, N. Nakagawa, A. Ohtomo, J. L. Grazul and H. Y. Hwang, *Nature*, 2004, **430**, 657-661.
10. J. Garcia-Barriocanal, A. Rivera-Calzada, M. Varela, Z. Sefrioui, E. Iborra, C. Leon, S. J. Pennycook and J. Santamaria, *Science*, 2008, **321**, 676-680.
11. A. V. Boris, Y. Matiks, E. Benckiser, A. Frano, P. Popovich, V. Hinkov, P. Wochner, M. Castro-Colin, E. Detemple, V. K. Malik, C. Bernhard, T. Prokscha, A. Suter, Z. Salman, E. Morenzoni, G. Cristiani, H. U. Habermeier and B. Keimer, *Science*, 2011, **332**, 937-940.
12. J. Chakhalian, J. W. Freeland, H. U. Habermeier, G. Cristiani, G. Khaliullin, M. van Veenendaal and B. Keimer, *Science*, 2007, **318**, 1114-1117.

13. J. Chakhalian, J. M. Rondinelli, J. Liu, B. A. Gray, M. Kareev, E. J. Moon, N. Prasai, J. L. Cohn, M. Varela, I. C. Tung, M. J. Bedzyk, S. G. Altendorf, F. Strigari, B. Dabrowski, L. H. Tjeng, P. J. Ryan and J. W. Freeland, *Phys. Rev. Lett.*, 2011, **107**, 116805.
14. H. Yamada, Y. Ogawa, Y. Ishii, H. Sato, M. Kawasaki, H. Akoh and Y. Tokura, *Science*, 2004, **305**, 646-648.
15. Y. W. Yin, J. D. Burton, Y. M. Kim, A. Y. Borisevich, S. J. Pennycook, S. M. Yang, T. W. Noh, A. Gruverman, X. G. Li, E. Y. Tsymbal and Q. Li, *Nat. Mater.*, 2013, **12**, 397-402.
16. Y.-M. Kim, A. Kumar, A. Hatt, A. N. Morozovska, A. Tselev, M. D. Biegalski, I. Ivanov, E. A. Eliseev, S. J. Pennycook, J. M. Rondinelli, S. V. Kalinin and A. Y. Borisevich, *Adv. Mater.*, 2013, **25**, 2497.
17. H. W. Jang, D. A. Felker, C. W. Bark, Y. Wang, M. K. Niranjan, C. T. Nelson, Y. Zhang, D. Su, C. M. Folkman, S. H. Baek, S. Lee, K. Janicka, Y. Zhu, X. Q. Pan, D. D. Fong, E. Y. Tsymbal, M. S. Rzchowski and C. B. Eom, *Science*, 2011, **331**, 886-889.
18. H. Lu, X. Liu, J. D. Burton, C. W. Bark, Y. Wang, Y. Zhang, D. J. Kim, A. Stamm, P. Lukashev, D. A. Felker, C. M. Folkman, P. Gao, M. S. Rzchowski, X. Q. Pan, C. B. Eom, E. Y. Tsymbal and A. Gruverman, *Adv. Mater.*, 2012, **24**, 1209-1216.
19. A. Y. Borisevich, H. J. Chang, M. Huijben, M. P. Oxley, S. Okamoto, M. K. Niranjan, J. D. Burton, E. Y. Tsymbal, Y. H. Chu, P. Yu, R. Ramesh, S. V. Kalinin and S. J. Pennycook, *Phys. Rev. Lett.*, 2010, **105**, 087204.
20. D. G. Schlom, L.-Q. Chen, C.-B. Eom, K. M. Rabe, S. K. Streiffer and J.-M. Triscone, *Annual Review of Materials Research*, 2007, **37**, 589-626.
21. H. Y. Hwang, Y. Iwasa, M. Kawasaki, B. Keimer, N. Nagaosa and Y. Tokura, *Nat. Mater.*, 2012, **11**, 103-113.
22. A. Bhattacharya and S. J. May, *Annual Review of Materials Research*, 2014, **44**, 65-90.
23. M. Bibes, J. E. Villegas and A. Barthélémy, *Advances in Physics*, 2011, **60**, 5-84.
24. P. Zubko, S. Gariglio, M. Gabay, P. Ghosez and J.-M. Triscone, *Annual Review of Condensed Matter Physics*, 2011, **2**, 141-165.
25. J. M. Rondinelli, S. J. May and J. W. Freeland, *MRS Bull.*, 2012, **37**, 261-270.
26. J. Chakhalian, J. W. Freeland, A. J. Millis, C. Panagopoulos and J. M. Rondinelli, *Reviews of Modern Physics*, 2014, **86**, 1189-1202.
27. J. M. Rondinelli and N. A. Spaldin, *Adv. Mater.*, 2011, **23**, 3363.
28. J. He, A. Borisevich, S. V. Kalinin, S. J. Pennycook and S. T. Pantelides, *Phys. Rev. Lett.*, 2010, **105**, 227203-227203.

29. J. M. Rondinelli and N. A. Spaldin, *Phys. Rev. B*, 2010, **82**, 113402.
30. K. J. Choi, S. H. Baek, H. W. Jang, L. J. Belenky, M. Lyubchenko and C.-B. Eom, *Adv. Mater.*, 2010, **22**, 759-762.
31. S. H. Chang, Y. J. Chang, S. Y. Jang, D. W. Jeong, C. U. Jung, Y. J. Kim, J. S. Chung and T. W. Noh, *Phys. Rev. B*, 2011, **84**, 104101.
32. D. Kan and Y. Shimakawa, *Crystal Growth & Design*, 2011, **11**, 5483-5487.
33. A. Vailionis, W. Siemons and G. Koster, *Appl. Phys. Lett.*, 2007, **91**, 071907-071907.
34. Z. H. Chen, A. R. Damodaran, R. Xu, S. Lee and L. W. Martin, *Appl. Phys. Lett.*, 2014, **104**, 182908.
35. H. Boschker, J. Kautz, E. P. Houwman, W. Siemons, D. H. A. Blank, M. Huijben, G. Koster, A. Vailionis and G. Rijnders, *Phys. Rev. Lett.*, 2012, **109**, 157207.
36. D. Samal, T. Haiyan, H. Molegraaf, B. Kuiper, W. Siemons, S. Bals, J. Verbeeck, G. Van Tendeloo, Y. Takamura, E. Arenholz, C. A. Jenkins, G. Rijnders and G. Koster, *Phys. Rev. Lett.*, 2013, **111**, 096102.
37. R. Aso, D. Kan, Y. Shimakawa and H. Kurata, *Scientific reports*, 2013, **3**, 2214.
38. R. Aso, D. Kan, Y. Shimakawa and H. Kurata, *Adv. Funct. Mater.*, 2014, **24**, 5177-5184.
39. R. Aso, D. Kan, Y. Shimakawa and H. Kurata, *Crystal Growth & Design*, 2014, **14**, 2128.
40. D. Kan, R. Aso, H. Kurata and Y. Shimakawa, *Adv. Funct. Mater.*, 2013, **23**, 1129-1136.
41. D. Kan, R. Aso, H. Kurata and Y. Shimakawa, *J. Appl. Phys.*, 2014, **115**, 184304.
42. D. Kan, R. Aso, H. Kurata and Y. Shimakawa, *J. Appl. Phys.*, 2013, **113**, 173912.
43. H. Fu and R. E. Cohen, *Nature*, 2000, **403**, 281-283.
44. K. M. Rabe, *Annual Review of Condensed Matter Physics*, 2010, **1**, 211-235.
45. J. M. Rondinelli and C. J. Fennie, *Adv. Mater.*, 2012, **24**, 1961-1968.
46. A. T. Mulder, N. A. Benedek, J. M. Rondinelli and C. J. Fennie, *Adv. Funct. Mater.*, 2013, **23**, 4810-4820.
47. H. Akamatsu, K. Fujita, T. Kuge, A. Sen Gupta, A. Togo, S. Lei, F. Xue, G. Stone, J. M. Rondinelli, L.-Q. Chen, I. Tanaka, V. Gopalan and K. Tanaka, *Phys. Rev. Lett.*, 2014, **112**, 187602.
48. T. Tanaka, K. Matsunaga, Y. Ikuhara and T. Yamamoto, *Phys. Rev. B*, 2003, **68**, 205213.
49. H. Akamatsu, Y. Kumagai, F. Oba, K. Fujita, K. Tanaka and I. Tanaka, *Adv. Funct. Mater.*, 2013, **23**, 1864-1872.
50. D. D. Fong, C. Cionca, Y. Yacoby, G. B. Stephenson, J. A. Eastman, P. H. Fuoss, S. K.

Streiffer, C. Thompson, R. Clarke, R. Pindak and E. A. Stern, *Phys. Rev. B*, 2005, **71**, 144112.

51. R. Herger, P. R. Willmott, C. M. Schlepütz, M. Björck, S. A. Pauli, D. Martoccia, B. D. Patterson, D. Kumah, R. Clarke, Y. Yacoby and M. Döbeli, *Phys. Rev. B*, 2008, **77**, 085401.
52. Y. Yamasaki, D. Okuyama, M. Nakamura, T.-h. Arima, M. Kawasaki, Y. Tokura, T. Kimura and Y. Wakabayashi, *J. Phys. Soc. Jpn.*, 2011, **80**, 073601.
53. R. Yamamoto, C. Bell, Y. Hikita, H. Y. Hwang, H. Nakamura, T. Kimura and Y. Wakabayashi, *Phys. Rev. Lett.*, 2011, **107**, 036104.
54. T. T. Fister, H. Zhou, Z. Luo, S. S. A. Seo, S. O. Hruszkewycz, D. L. Proffit, J. A. Eastman, P. H. Fuoss, P. M. Baldo, H. N. Lee and D. D. Fong, *APL Materials*, 2014, **2**, 021102.
55. P. R. Willmott, S. A. Pauli, R. Herger, C. M. Schlepütz, D. Martoccia, B. D. Patterson, B. Delley, R. Clarke, D. Kumah, C. Cionca and Y. Yacoby, *Phys. Rev. Lett.*, 2007, **99**, 155502.
56. S. J. May, J. W. Kim, J. M. Rondinelli, E. Karapetrova, N. A. Spaldin, A. Bhattacharya and P. J. Ryan, *Phys. Rev. B*, 2010, **82**, 014110.
57. R. L. Johnson-Wilke, D. Marincel, S. Zhu, M. P. Warusawithana, A. Hatt, J. Sayre, K. T. Delaney, R. Engel-Herbert, C. M. Schlepütz, J. W. Kim, V. Gopalan, N. A. Spaldin, D. G. Schlom, P. J. Ryan and S. Trolier-McKinstry, *Phys. Rev. B*, 2013, **88**, 174101.
58. S. J. May, C. R. Smith, J. W. Kim, E. Karapetrova, A. Bhattacharya and P. J. Ryan, *Phys. Rev. B*, 2011, **83**, 153411-153411.
59. H. Rotella, U. Lüders, P. E. Janolin, V. H. Dao, D. Chateigner, R. Feyerherm, E. Dudzik and W. Prellier, *Phys. Rev. B*, 2012, **85**, 184101.
60. W. Lu, P. Yang, W. D. Song, G. M. Chow and J. S. Chen, *Phys. Rev. B*, 2013, **88**, 214115.
61. A. Vailionis, H. Boschker, W. Siemons, E. P. Houwman, D. H. A. Blank, G. Rijnders and G. Koster, *Phys. Rev. B*, 2011, **83**, 064101-064101.
62. R. Aso, D. Kan, Y. Fujiyoshi, Y. Shimakawa and H. Kurata, *Crystal Growth & Design*, 2014, **14**, 6478-6485.
63. Y. Shao-Horn, L. Croguennec, C. Delmas, E. C. Nelson and M. A. O'Keefe, *Nat. Mater.*, 2003, **2**, 464-467.
64. C.-L. Jia, V. Nagarajan, J.-Q. He, L. Houben, T. Zhao, R. Ramesh, K. Urban and R. Waser, *Nat. Mater.*, 2007, **6**, 64-69.
65. C. L. Jia, M. Lentzen and K. Urban, *Science*, 2003, **299**, 870-873.
66. C.-L. Jia, S.-B. Mi, K. Urban, I. Vrejoiu, M. Alexe and D. Hesse, *Nat. Mater.*, 2008, **7**,

57-61.

67. C. L. Jia, S. B. Mi, M. Faley, U. Poppe, J. Schubert and K. Urban, *Phys. Rev. B*, 2009, **79**, 081405.
68. A. Borisevich, O. S. Ovchinnikov, H. J. Chang, M. P. Oxley, P. Yu, J. Seidel, E. A. Eliseev, A. N. Morozovska, R. Ramesh, S. J. Pennycook and S. V. Kalinin, *ACS Nano*, 2010, **4**, 6071-6079.
69. Z. Wang, L. Gu, M. Saito, S. Tsukimoto, M. Tsukada, F. Lichtenberg, Y. Ikuhara and J. G. Bednorz, *Adv. Mater.*, 2013, **25**, 218-222.
70. J. Hwang, J. Y. Zhang, J. Son and S. Stemmer, *Appl. Phys. Lett.*, 2012, **100**, 19190.
71. J. Y. Zhang, J. Hwang, S. Raghavan and S. Stemmer, *Phys. Rev. Lett.*, 2013, **110**, 256401.
72. S. D. Findlay, N. Shibata, H. Sawada, E. Okunishi, Y. Kondo, T. Yamamoto and Y. Ikuhara, *Appl. Phys. Lett.*, 2009, **95**, 191913.
73. S. D. Findlay, N. Shibata, H. Sawada, E. Okunishi, Y. Kondo and Y. Ikuhara, *Ultramicroscopy*, 2010, **110**, 903-923.
74. M. Haruta and H. Kurata, *Scientific reports*, 2012, **2**, 252.
75. S. J. Pennycook and D. E. Jesson, *Phys. Rev. Lett.*, 1990, **64**, 938-941.
76. S. J. Pennycook and D. E. Jesson, *Ultramicroscopy*, 1991, **37**, 14-38.
77. M. Saito, K. Kimoto, T. Nagai, S. Fukushima, D. Akahoshi, H. Kuwahara, Y. Matsui and K. Ishizuka, *J. Electron Microsc.*, 2009, **58**, 131-136.
78. P. L. Galindo, S. Kret, A. M. Sanchez, J.-Y. Laval, A. Yáñez, J. Pizarro, E. Guerrero, T. Ben and S. I. Molina, *Ultramicroscopy*, 2007, **107**, 1186-1193.
79. J. P. Pedro Galindo, Sergio Molina and Kazuo Ishizuka, *Microsc. Anal.*, 2009, **23**, 23.
80. G. Koster, L. Klein, W. Siemons, G. Rijnders, J. S. Dodge, C.-B. Eom, D. H. A. Blank and M. R. Beasley, *Reviews of Modern Physics*, 2012, **84**, 253-298.
81. A. M. Glazer, *Acta Crystallographica Section B*, 1972, **28**, 3384-3392.
82. C. W. Jones, P. D. Battle, P. Lightfoot and W. T. A. Harrison, *Acta Crystallographica Section C*, 1989, **45**, 365-367.
83. R. P. Liferovich and R. H. Mitchell, *J. Solid State Chem.*, 2004, **177**, 2188-2197.
84. J. E. Kleibeuker, G. Koster, W. Siemons, D. Dubbink, B. Kuiper, J. L. Blok, C.-H. Yang, J. Ravichandran, R. Ramesh, J. E. ten Elshof, D. H. A. Blank and G. Rijnders, *Adv. Funct. Mater.*, 2010, **20**, 3490-3496.
85. D. L. Proffit, H. W. Jang, S. Lee, C. T. Nelson, X. Q. Pan, M. S. Rzchowski and C. B. Eom, *Appl. Phys. Lett.*, 2008, **93**, 111912.
86. E. J. Moon, P. V. Balachandran, B. J. Kirby, D. J. Keavney, R. J. Sichel-Tissot, C. M. Schlepütz, E. Karapetrova, X. M. Cheng, J. M. Rondinelli and S. J. May, *Nano Lett.*,

2014, **2014**, 2509-2514.

87. M. D. Biegalski, Y. Takamura, A. Mehta, Z. Gai, S. V. Kalinin, H. Ambaye, V. Lauter, D. Fong, S. T. Pantelides, Y. M. Kim, J. He, A. Borisevich, W. Siemons and H. M. Christen, *Advanced Materials Interfaces*, 2014, **1**, 1400203.
88. A. Vailionis, H. Boschker, Z. Liao, J. R. A. Smit, G. Rijnders, M. Huijben and G. Koster, *Appl. Phys. Lett.*, 2014, **105**, 131906.
89. G. Cao, S. McCall, M. Shepard, J. E. Crow and R. P. Guertin, *Phys. Rev. B*, 1997, **56**, 321-329.
90. A. Kanbayasi, *J. Phys. Soc. Jpn.*, 1976, **41**, 1876-1878.
91. A. Kanbayasi, *J. Phys. Soc. Jpn.*, 1978, **44**, 89-95.
92. Y. Kats, I. Genish, L. Klein, J. W. Reiner and M. R. Beasley, *Phys. Rev. B*, 2005, **71**, 100403-100403.
93. P. M. Woodward, *Acta Crystallographica Section B*, 1997, **53**, 32-43.
94. J. B. Goodenough, *Rep. Prog. Phys.*, 2004, **67**, 1915.
95. E. J. Moon, R. Colby, Q. Wang, E. Karapetrova, C. M. Schlepütz, M. R. Fitzsimmons and S. J. May, *Nat Commun*, 2014, **5**.
96. T. Yajima, Y. Hikita and H. Y. Hwang, *Nat. Mater.*, 2011, **10**, 198-201.
97. A. Chanthbouala, A. Crassous, V. Garcia, K. Bouzehouane, S. Fusil, X. Moya, J. Allibe, B. Dlubak, J. Grollier, S. Xavier, C. Deranlot, A. Moshar, R. Proksch, N. D. Mathur, M. Bibes and A. Barthelemy, *Nat. Nano.*, 2012, **7**, 101-104.
98. E. Y. Tsymbal, A. Gruverman, V. Garcia, M. Bibes and A. Barthélémy, *MRS Bull.*, 2012, **37**, 138-143.
99. A. Sawa, *Mater. Today*, 2008, **11**, 28-36.

Figure Captions

Fig. 1: Crystal structures of $SrRuO_3$ (SRO, top) and $GdScO_3$ (GSO, bottom). Both oxides have *Pbmn* orthorhombic structures with the octahedral tilts described as $a^-a^-c^+$ in the Glazer notation. In the figure, the A-site cations are omitted for clarity. When SRO is epitaxially grown on the GSO substrate, the oxygen atoms at the SRO/GSO heterointerface would be additionally displaced so as to maintain the corner-connection between the RuO_6 and ScO_6 octahedra by sharing the oxygen atoms (as indicated by the red arrows). The θ_{tilt} used in this study corresponds to the value projected on the $(001)_{ortho}$ plane.

Fig. 2: HAADF- and ABF-STEM observations for the monoclinic-SRO/GSO (m-SRO/GSO) heterostructure. (a) High-resolution HAADF image taken along the $[001]_{ortho}$ direction. Simulated HAADF images of bulk SRO and GSO are inserted in the image. (b) HAADF intensity profiles of A- (left side) and B-site (right side) cations across the interface. The A- and B-site profiles were collected along the red and blue lines in the HAADF image (Fig. 2a), respectively. The orange line denotes for the position of the SRO/GSO heterointerface at which the substrate is terminated by the ScO_2 layer. (c) ABF image taken from the same region as the HAADF image (Fig. 2a). In the ABF image, the oxygen atoms are clearly seen, providing information on how the oxygen octahedra are connected across the heterostructure as indicated with the red squares.

Fig. 3: Quantitative analysis of octahedral distortions in the SRO/GSO heterostructures. Variations in the out-of-plane lattice spacing d_{out} (circle) and out-of-plane octahedral tilt angle θ_{tilt} (filled square) and in-plane θ_{tilt} (open square) in the (a) monoclinic-SRO/GSO and (b) tetragonal-SRO/GSO heterostructures. The d_{out} and θ_{tilt} values were extracted from the HAADF and ABF images, respectively. The bulk counterparts of d_{out} and θ_{tilt} for the SRO (a_{pc_SRO} = 3.92 Å, θ_{tilt_SRO} = 168°)[82]

and GSO (a_{pc_GSO} = 3.96 Å, θ_{tilt_GSO} = 156°)[83] are indicated by black and pink lines, respectively. The orange dashed line represents the position of the SRO/GSO interface. The error bars correspond to the standard deviation of each determined values.

Fig. 4: Atomic-level structural characterizations at the SRO/GSO heterointerface. (a) Variations of in-plane oxygen displacement Δx in the monoclinic-SRO/GSO (m-SRO/GSO) and tetragonal-SRO/GSO (t-SRO/GSO) heterostructures. The oxygen displacement Δx is defined as the distance from the middle position between A-site cations along the in-plane direction and was extracted from the ABF images. The oxygen displacements in bulk SRO (Δx_{SRO} = 21 pm) and GSO (Δx_{GSO} = 43 pm) are also shown with black and pink lines, respectively. (b) Schematic drawings of the oxygen octahedral connections across the m-SRO/GSO and t-SRO/GSO heterointerfaces. Whereas the in-plane lattice spacing for both m- and t-SRO layers are identical to that of the GSO substrates, the in-plane oxygen displacement Δx at the SRO/GSO interface depends on the structure of the SRO layer as highlighted with the yellow boxes.

Fig. 5: Magneto-transport characterizations of the SRO/GSO heterostructures. (a) Typical magnetic field dependence of Hall resistivity ρ_{xy} of the m-SRO/GSO and t-SRO/GSO heterostructures. The data were taken at 10 K. For the measurements, the current and magnetic field were applied along the $[001]_{GSO}$ and $[110]_{GSO}$ directions, respectively. (b and c) Magnetic field angle θ_H dependence of the Hall resistivity ρ_{xy} of (b) m-SRO/GSO and (c) t-SRO/GSO heterostructures. (d) Magnetic easy axis angle α as a function of the SRO layer thickness.

Fig. 6: Schematic illustration for phase control of SRO layer through the interface engineering of oxygen displacement. By inserting the one-unit-cell-thick $BaTiO_3$ (BTO) layer with non-tilted TiO_6

octahedra, the displacement of the oxygen at the heterointerface is largely suppressed and consequently the octahedral tilt propagation from the GSO substrate is blocked at the interface. This stabilizes the tetragonal SRO layer, unlike the monoclinic one that is seen when the SRO layer (below 16 nm) is directly grown on the GSO substrate.

Fig. 7: Fabrications and structural characterizations of the SRO/BTO/GSO heterostructure. (a) Changes in the RHEED spot intensity during the deposition of the one-unit-cell-thick BTO layer on the GSO substrate. In the bottom shown are the RHEED patterns for the GSO substrate (boxed in pink) and the one-unit-cell-thick BTO layer on the substrate (boxed in cyan). The patterns were taken at 700 ºC. (b) X-ray reciprocal space mappings taken for the (b) m-SRO/GSO and (c) SRO/1u.c.BTO/GSO heterostructures. The subscripts *pc* and *o* denote for the pseudocubic and orthorhombic perovskite notations, respectively.

Fig. 8: HAADF-STEM characterizations for the SRO/1u.c.BTO/GSO heterostructure. (a) HAADF-STEM image of the SRO/1u.c.BTO/GSO heterostructure. The image was taken along the $[001]_{ortho}$ direction. (b) HAADF intensity profiles of the A- and B-site cations in the heterostructure. The intensities of the A- and B-site cations were collected along the red and blue dashed lines in (a), respectively.

Fig. 9: ABF-STEM characterizations for the SRO/1u.c.BTO/GSO heterostructure. (a) ABF-STEM image of the SRO/1u.c.BTO/GSO heterostructure. (b and c) Changes in (b) the octahedral tilt angle θ_{tilt} and (c) in-plane oxygen displacement Δx across the heterostructure. In (b) and (c), the lines in black and purple corresponds to the parameters of the SRO ($\theta_{tilt\_SRO\_bulk} = 168^{o}$ and Δx = 21 pm) and GSO ($\theta_{tilt\_GSO\_bulk} = 156^{o}$ and Δx = 43 pm) in bulk, respectively. The error bars in the figures

represent the standard deviation for each determined value.

Fig. 10: Magneto-transport characterizations of the SRO/BTO/GSO heterostructures. (a) Magnetic field dependence of Hall resistivity ρ_{xy} of the SRO/1u.c.BTO/GSO heterostructure at 10 K. For comparison, the magnetic field dependence of ρ_{xy} for the m-SRO/GSO heterostructure is also plotted. For the measurements, the current and magnetic field were applied along the $[001]_{GSO}$ and $[110]_{GSO}$ directions, respectively. (b) In-plane magnetic field angle dependence of ρ_{xx} for the SRO/1u.c.BTO/GSO heterostructure at 10 K. The 0.4-Tesla magnetic field was rotated in the $(110)_{ortho}$ plane, and the currents were applied along the $[1\text{–}10]_{ortho}$ direction of the substrate. The definition of the field angle θ_H is given in the figure. (c) Temperature dependence of the magnetic easy axis (E_a) direction α of the SRO layer in the m-SRO/GSO and SRO/1u.c.BTO/GSO heterostructures. For the m-SRO/GSO heterostructure, the magnetic E_a direction was determined from the magnetic field angle dependence of ρ_{xy} under the magnetic field in the $(001)_{ortho}$ plane as shown in Fig. 5b. (d) E_a direction α of the SRO layer as a function of the BTO layer thickness between SRO and GSO.

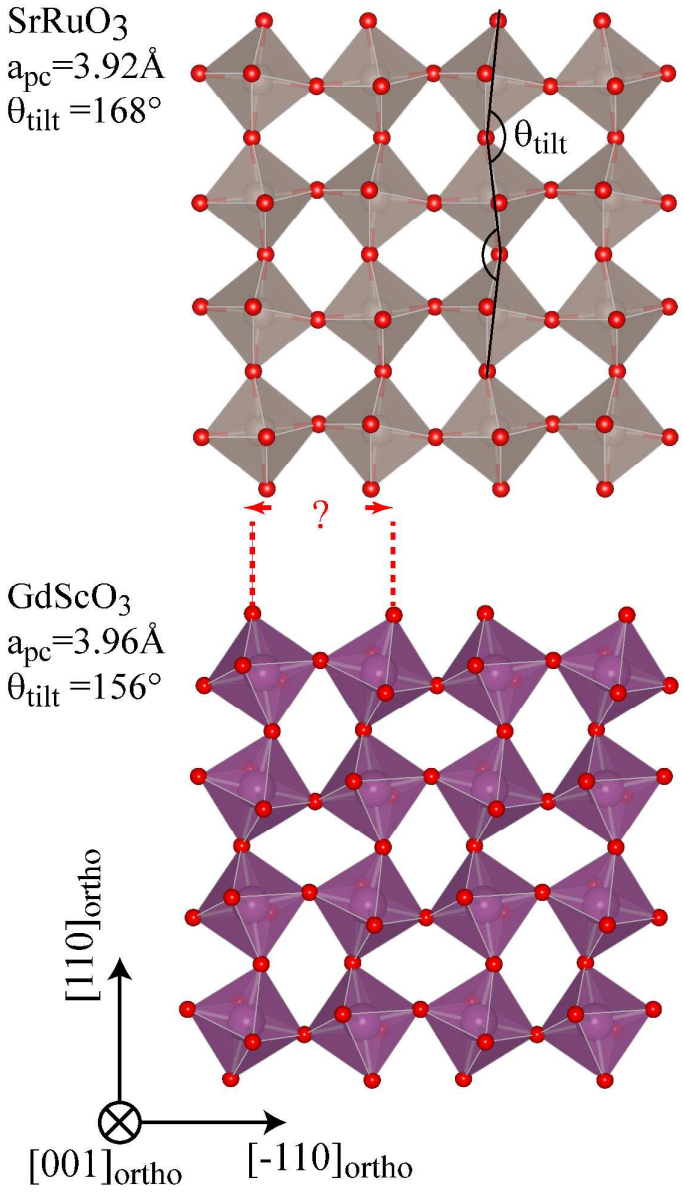

Figure 1

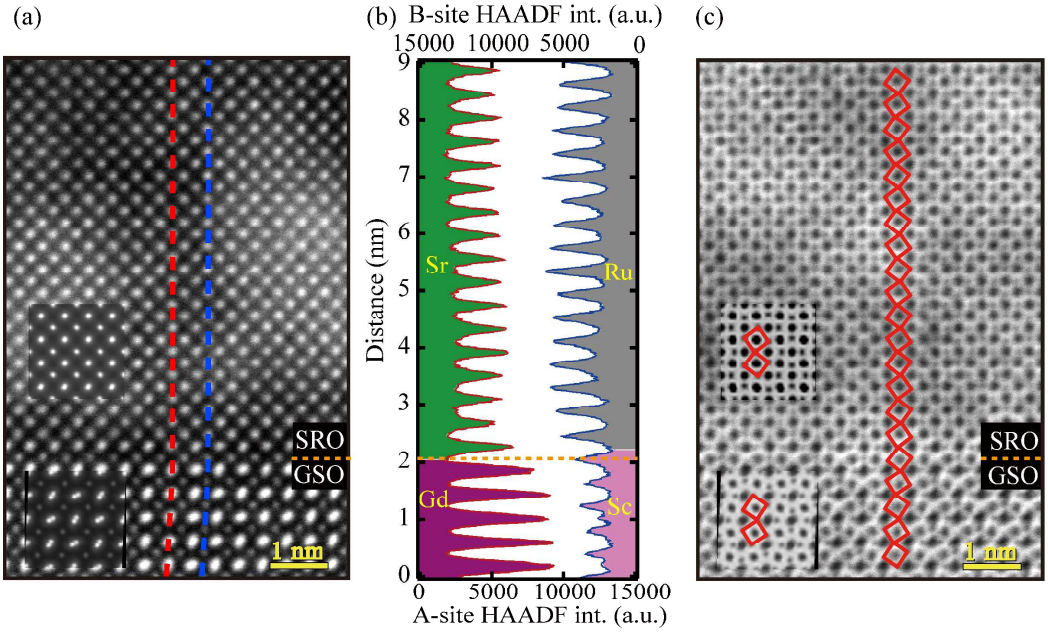

Figure 2

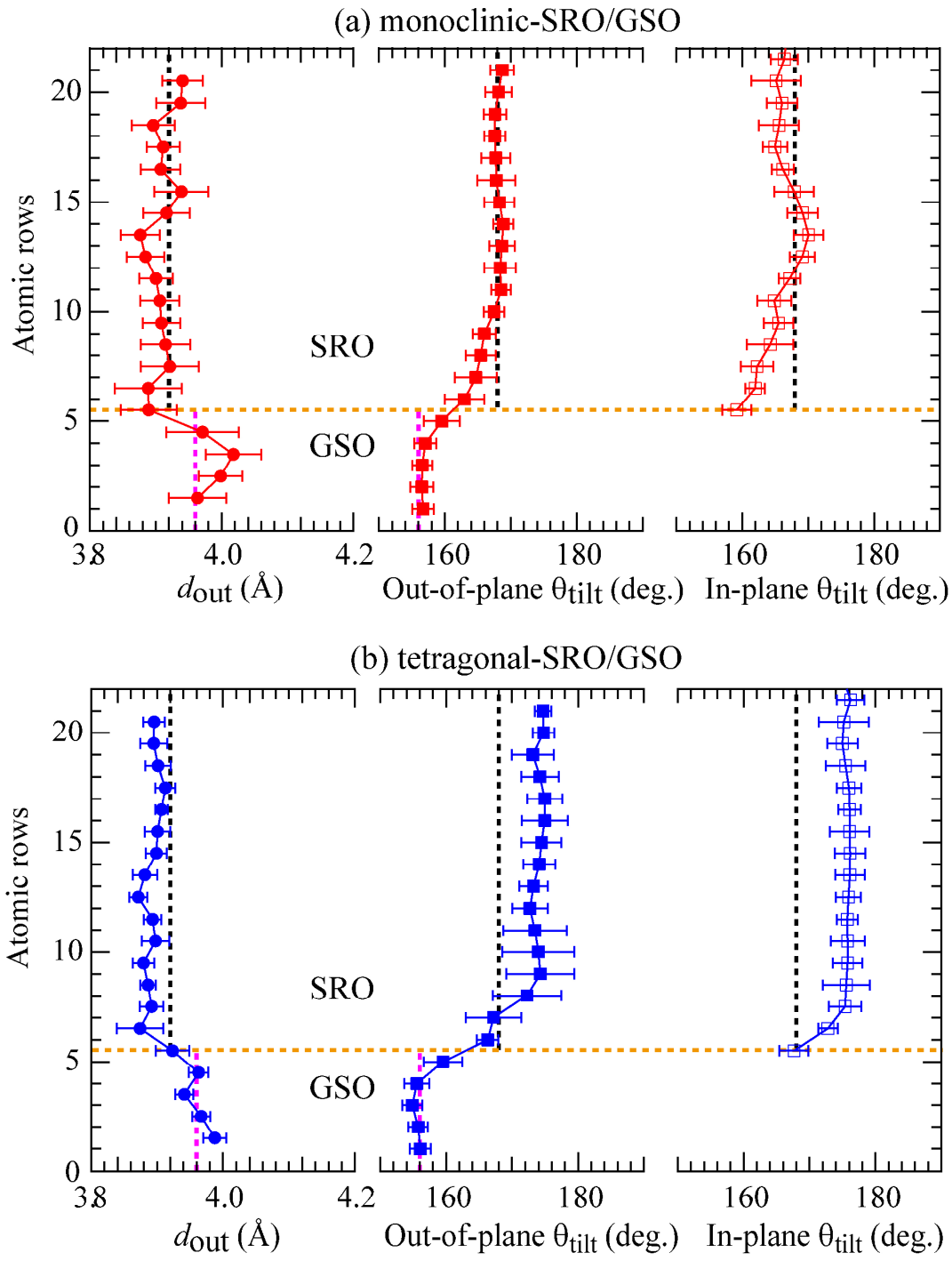

Figure 3

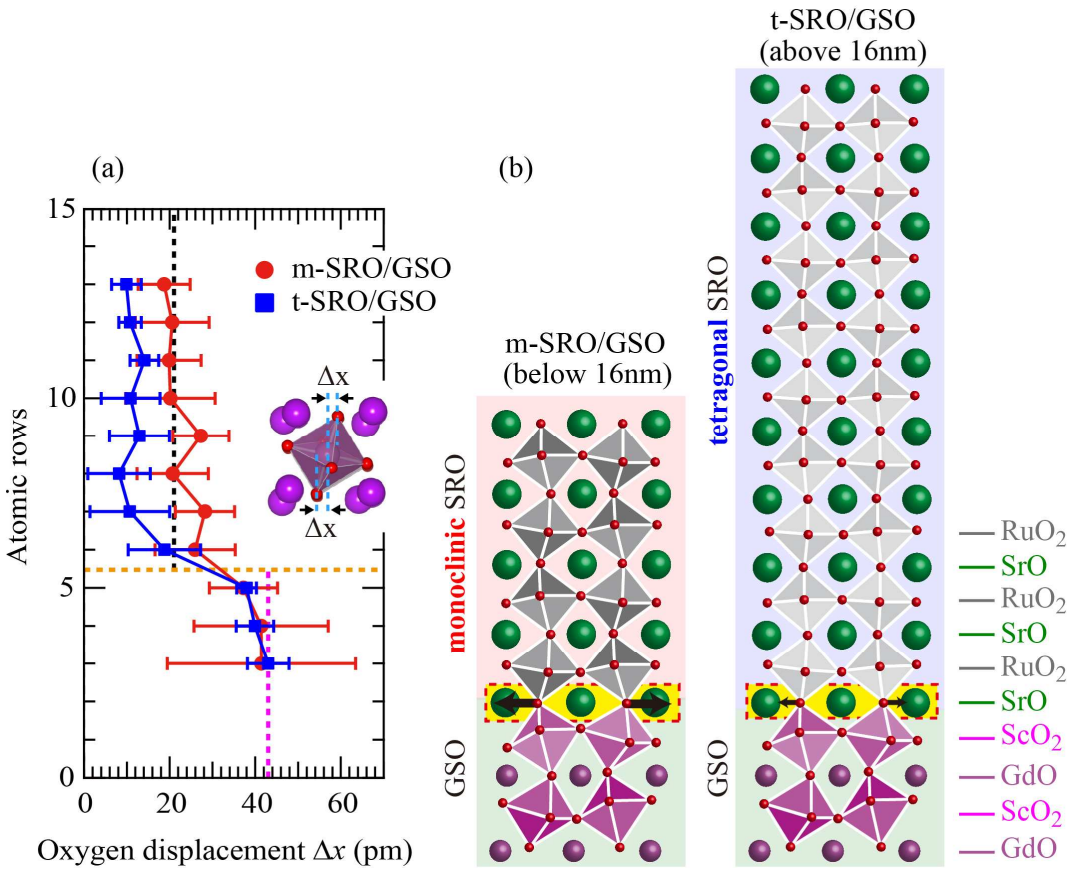

Figure 4

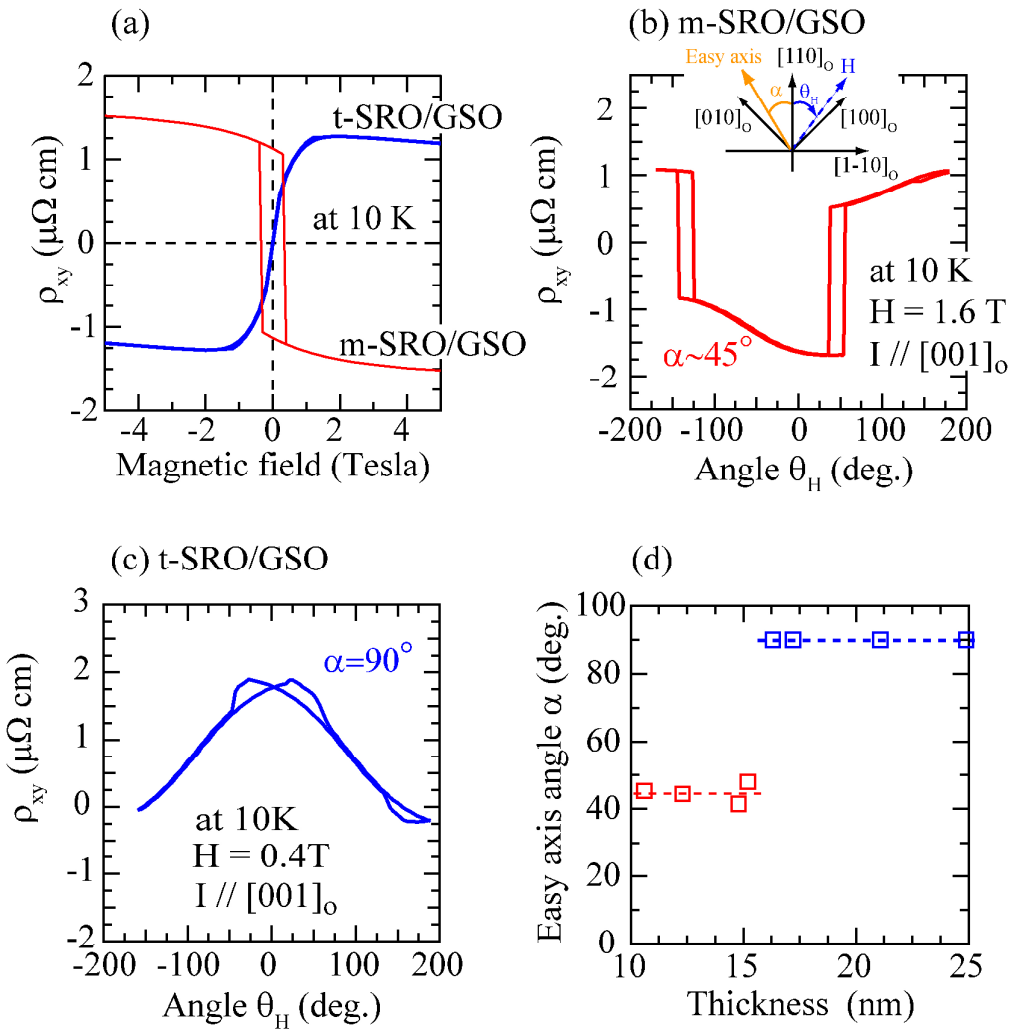

Figure 5

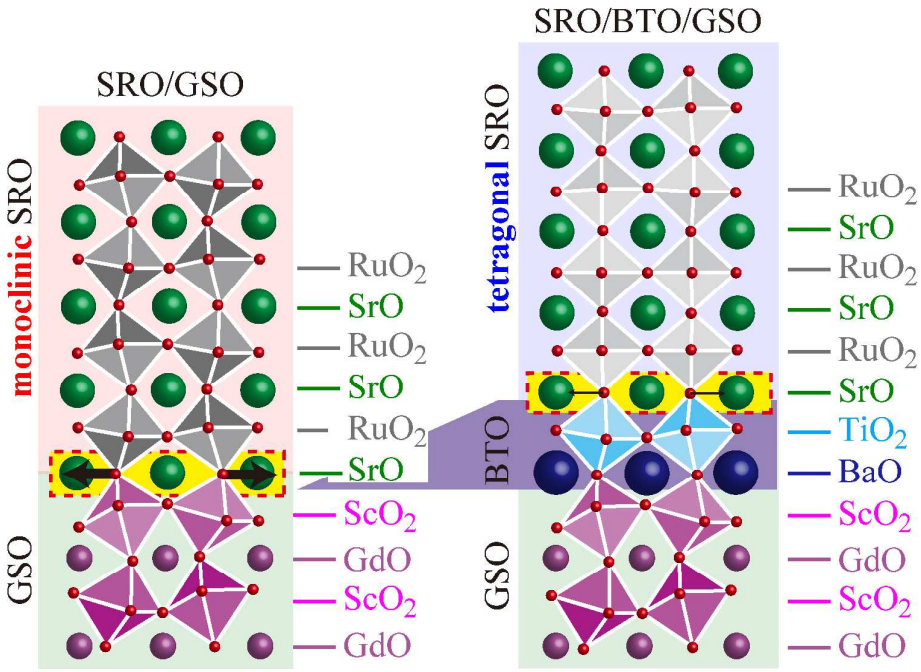

Figure 6

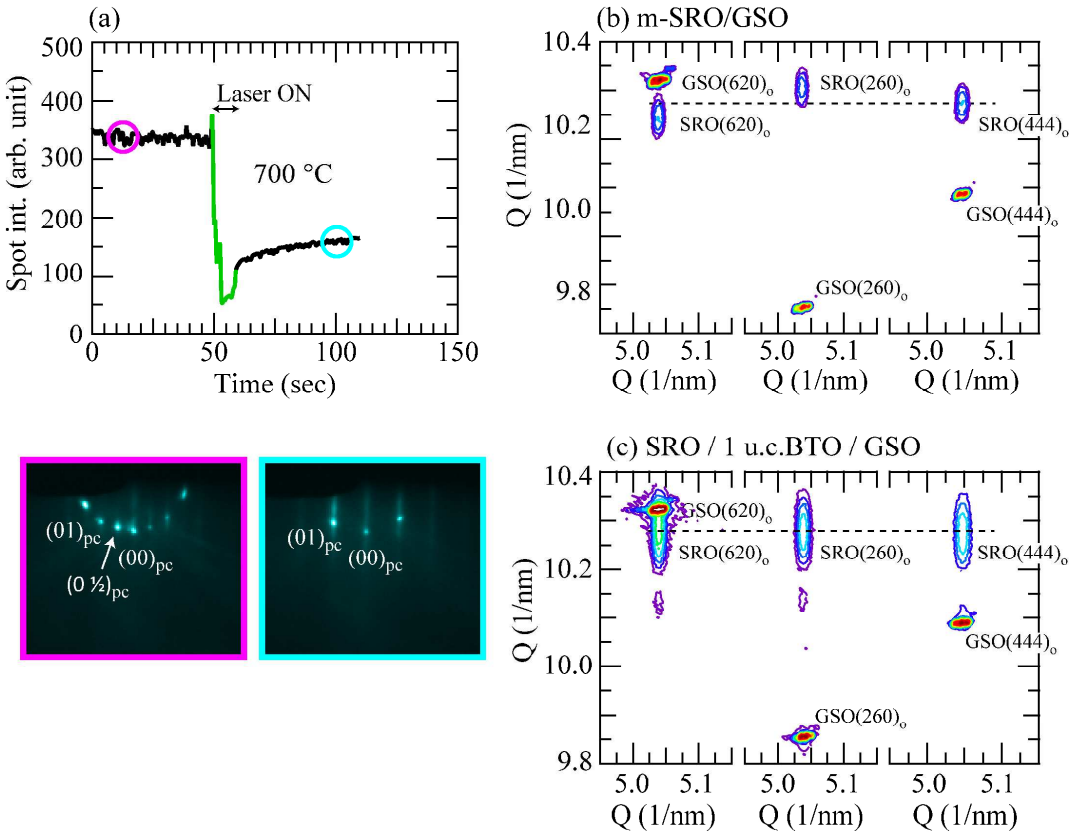

Figure 7

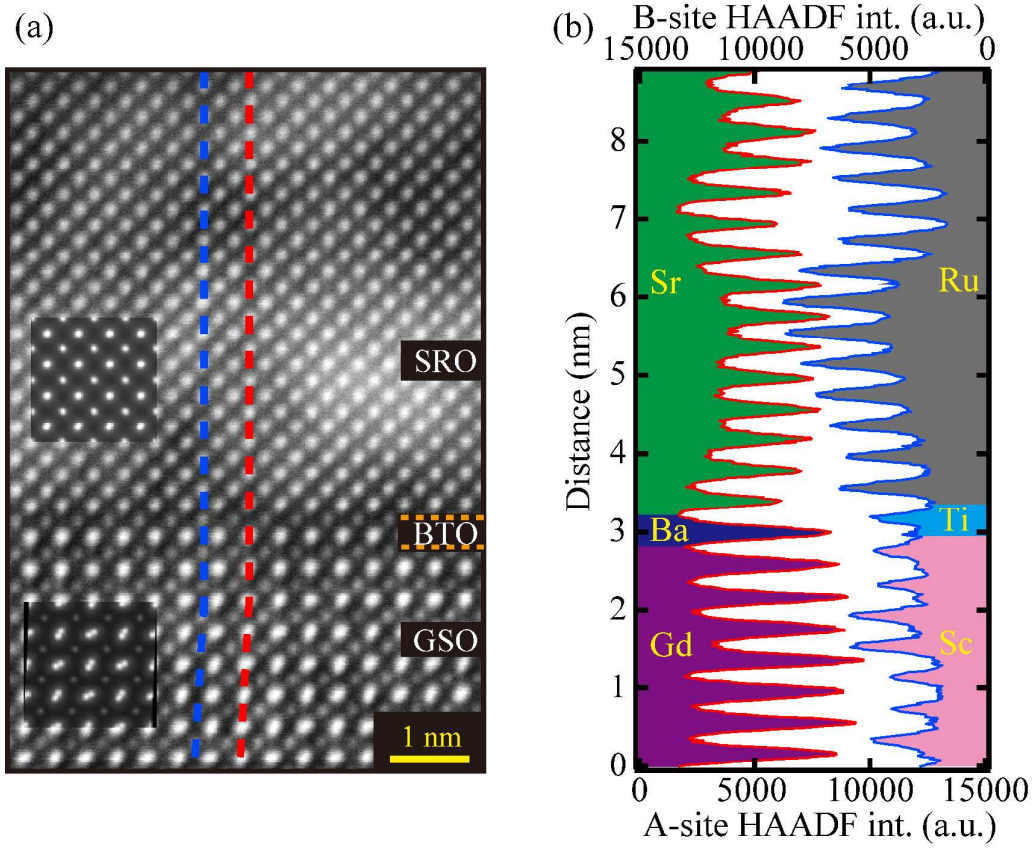

Figure 8

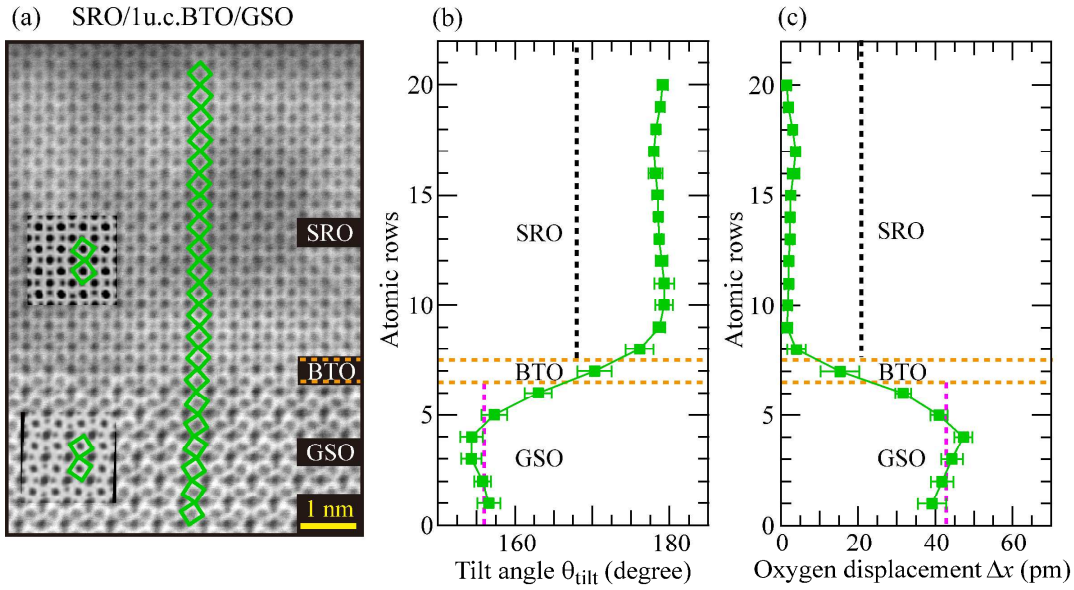

Figure 9

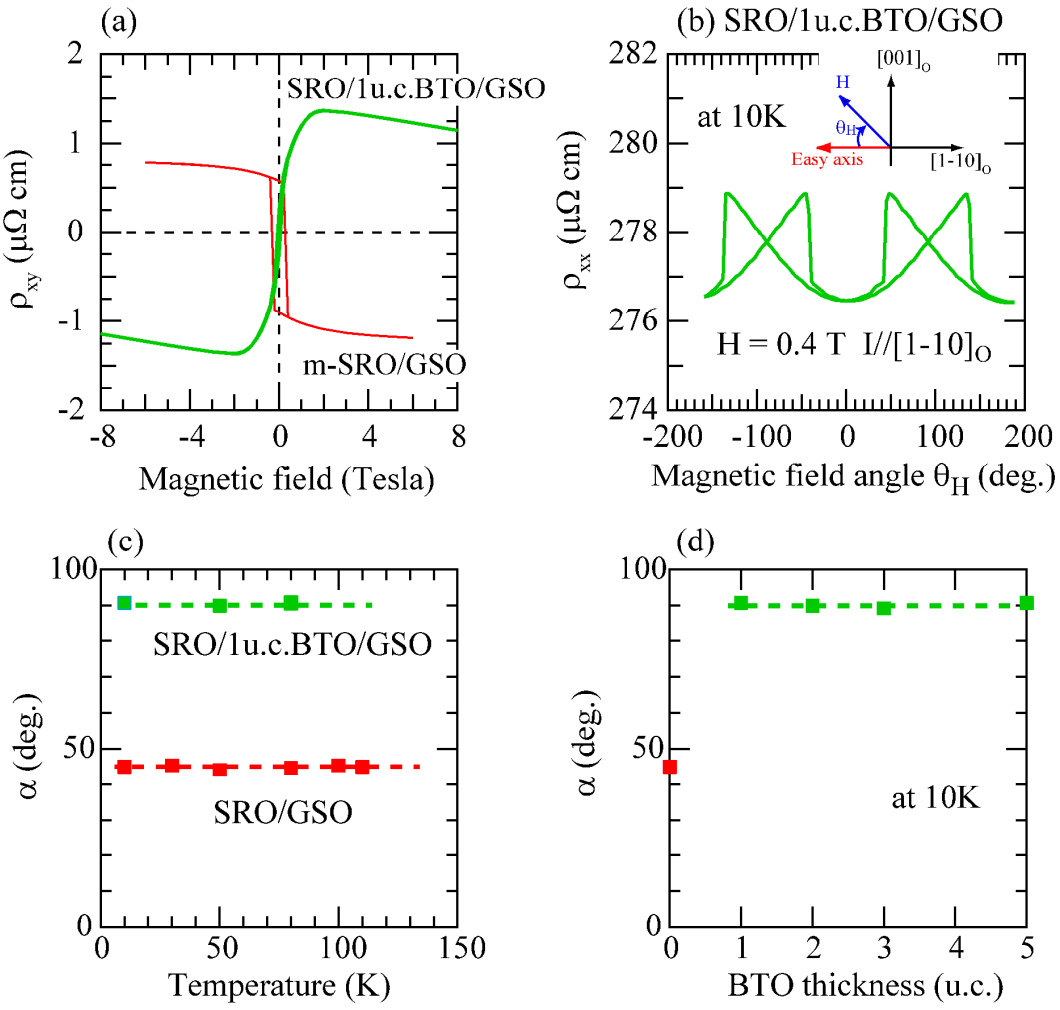

Figure 10

We overview investigations highlighting the significance of interface engineering of oxygen displacement as a tool for phase control of strained oxides.